



## PAPER

[View Article Online](#)  
[View Journal](#) | [View Issue](#)


Cite this: *Green Chem.*, 2023, **25**, 6315

# An efficient, green, and residual oxidant-free wastewater treatment technique enabled by coupling a dual-cathode heterogeneous electro-Fenton process and UV radiation in tandem†

Lele Cui, <sup>a,b,c</sup> Mingming Sun<sup>a,b,c</sup> and Zhenghua Zhang <sup>\*a,b,c</sup>

Efficient implementation of a catalyst-integrated cathode-based heterogeneous electro-Fenton (HEF) process usually suffers from the conflict between the optimal potentials of the two targeted reduction reactions ( $\text{O}_2$  to  $\text{H}_2\text{O}_2$  and  $\text{metal}^{(n+1)+}$  to  $\text{metal}^{(n)+}$ ). In addition, the residual  $\text{H}_2\text{O}_2$  in the HEF effluent poses a potential environmental risk to aquatic ecosystems and would further make the HEF technology impractical. Herein, a tandem system of dual-cathode HEF and UV radiation is proposed to bypass these issues. In the dual-cathode HEF unit, the air-diffusion cathode (ADC) without aeration and the FeOCl-functionalized graphite felt (FeOCl/GF) perform their respective functions at different operating current densities ( $100 \text{ mA cm}^{-2}$  for ADC and  $5 \text{ mA cm}^{-2}$  for FeOCl/GF) to achieve efficient  $\text{H}_2\text{O}_2$  production,  $\cdot\text{OH}$  formation and Fe(III) electroreduction simultaneously. Subsequently, the underutilized  $\text{H}_2\text{O}_2$  in the HEF effluent will be reactivated in the UV module to eliminate the risk of oxidant residues while further improving the decontamination efficiency. Importantly, interesting antagonistic and synergistic phenomena governed by the cathodic current density of the ADC in this tandem system were also highlighted by constructing different standalone/coupled processes. The HEF/UV tandem strategy proposed in the present work offers a promising scheme for distributed wastewater treatment due to the demonstrated preminent process efficiency, as well as the reagent- and residual-oxidant-free green chemistry concept.

Received 17th May 2023,  
Accepted 13th July 2023

DOI: 10.1039/d3gc01653f

[rsc.li/greenchem](http://rsc.li/greenchem)

## 1. Introduction

Decentralized water treatment systems with small-scale characteristics offer a promising means of accessing clean water, as they theoretically substantially reduce the energy input while enabling the fulfillment of various end-user-specific treatment needs.<sup>1,2</sup> Unfortunately, the challenge of anthropogenically exacerbated accumulation of persistent organic pollutants (POPs) in aquatic ecosystems makes distributed schemes impractical, due to the rather inefficient decontamination performance of conventional wastewater treatment facilities for POPs.<sup>2,3</sup> Electrochemical advanced oxidation processes

(EAOPs), capable of degrading most hazardous organic compounds, are appealing module options for such decentralized systems.<sup>4</sup> Among the EAOP family, those based on the Fenton reaction chemistry, such as electro-Fenton (EF), have proven to be the most robust techniques.<sup>5,6</sup> The efficiency of the EF process lies in the generation of strongly oxidizing hydroxyl radicals ( $\cdot\text{OH}$ ) *via* the Fenton reaction between the cathode-produced hydrogen peroxide ( $\text{H}_2\text{O}_2$ ) and the externally added  $\text{Fe}^{2+}$  catalyst.<sup>4,7</sup> Nevertheless, the conventional homogeneous EF process suffers from fundamental drawbacks, such as a narrow working pH window (2.8–3.5) and the formation of iron sludge.<sup>8</sup> In this context, heterogeneous EF (HEF) with solid-phase iron catalyst-functionalized carbonaceous cathode supports has recently been extensively developed and validated to effectively overcome these bottlenecks while bypassing the time-consuming and costly dispersion/separation procedures of catalyst particles in typical suspended heterogeneous processes.<sup>4,6</sup>

Over the past few years, substantial efforts have focused on the rational design of advanced catalytic cathodes to maximize the production of  $\cdot\text{OH}$ , such as heteroatom-incorporated spinel-grafted carbon fibers,<sup>9</sup> transition metal-encapsulated

<sup>a</sup>Membrane & Nanotechnology-Enabled Water Treatment Center, Institute of Environment and Ecology, Tsinghua Shenzhen International Graduate School, Tsinghua University, Shenzhen 518055, Guangdong, China.

E-mail: [zhenghua.zhang@sz.tsinghua.edu.cn](mailto:zhenghua.zhang@sz.tsinghua.edu.cn)

<sup>b</sup>Guangdong Provincial Engineering Research Centre for Urban Water Recycling and Environmental Safety, Tsinghua Shenzhen International Graduate School, Tsinghua University, Shenzhen, 518055 Guangdong, China

<sup>c</sup>School of Environment, Tsinghua University, Beijing 100084, China

†Electronic supplementary information (ESI) available. See DOI: <https://doi.org/10.1039/d3gc01653f>

carbon aerogels,<sup>10</sup> and even atomically dispersed iron-anchored porous carbons.<sup>11</sup> Despite these encouraging achievements, the reaction kinetics of HEF processes are generally significantly inferior (at least by one order of magnitude) to their homogeneous counterparts at equivalent catalyst loadings.<sup>12</sup> In addition to the inherent limited atom utilization of solid catalysts, this phenomenon may also be closely related to the difficulty in executing the expected dual functions (*i.e.*, generation of H<sub>2</sub>O<sub>2</sub> and <sup>•</sup>OH in a stepwise manner) of such composite cathodes in real working scenarios. For one thing, most foreign metal species were identified as being thermodynamically more favorable for the 4e<sup>−</sup> pathway (O<sub>2</sub> + 4H<sup>+</sup> + 4e<sup>−</sup> → 2H<sub>2</sub>O) than the 2e<sup>−</sup> pathway (O<sub>2</sub> + 2H<sup>+</sup> + 2e<sup>−</sup> → H<sub>2</sub>O<sub>2</sub>) during the oxygen reduction reaction (ORR), which would cause deterioration of H<sub>2</sub>O<sub>2</sub> production in the system.<sup>6,10,13</sup> Although previous reports have attributed the observed drop in H<sub>2</sub>O<sub>2</sub> yield entirely to an on-site activation mechanism,<sup>14,15</sup> this has not been subjected to rigorous molecular-level justification due to the hitherto elusive interaction between the catalyst and the carbon matrix in the ORR. For another, such integrated cathode-catalyzed HEF processes generally suffer from the working current density problem, namely the mismatch of the required potentials for H<sub>2</sub>O<sub>2</sub> generation (*E*<sup>o</sup> = 0.695 V per SHE) and high-valent metal electroreduction (*E*<sup>o</sup> = 0.77 V per SHE for Fe(III)).<sup>16,17</sup> As a result, it is difficult to achieve optimal H<sub>2</sub>O<sub>2</sub> production and active metal regeneration as well as <sup>•</sup>OH formation simultaneously in conventional operation with a single cathode. Although there are several recent studies of homogeneous EF designed dual-cathode systems to cope with this bottleneck, they were not green and sustainable due to the necessity of either complex iron salt dosing or costly oxygen/air aeration procedures.<sup>12,16,18</sup>

Another important but underappreciated issue is that most of the current works exclusively pursue high decontamination efficiency without concern for the residual H<sub>2</sub>O<sub>2</sub> in the HEF effluent. Indeed, excessive accumulation of H<sub>2</sub>O<sub>2</sub> at the end of EF treatment was frequently detected, either for homogeneous or heterogeneous modes,<sup>4,14,19</sup> which not only causes an undesired wastage of electrical energy but also poses a potential risk to aquatic organisms and phytoplankton if the effluent is discharged directly.<sup>20</sup> A recent endeavor couples a HEF system with a Fe<sub>3</sub>O<sub>4</sub>-carbon filter to quench residual H<sub>2</sub>O<sub>2</sub> and thus makes the effluent safe for discharge into the environment.<sup>21</sup> However, this process relies on the catalytic disproportionation of H<sub>2</sub>O<sub>2</sub> to O<sub>2</sub> by the Fe<sub>3</sub>O<sub>4</sub>-carbon filter, resulting in a decrease in H<sub>2</sub>O<sub>2</sub> utilization and potential secondary pollution by Fe leaching. UV/H<sub>2</sub>O<sub>2</sub> is a well-established technique in potable water facilities, which can effectively remove trace organic contaminants by <sup>•</sup>OH generated from the photolytic homolysis of H<sub>2</sub>O<sub>2</sub>.<sup>3,19</sup> More strikingly, benefiting from its excellent activation efficiency, even a low concentration of H<sub>2</sub>O<sub>2</sub> (*e.g.*, 3 mg L<sup>−1</sup>) can still be rapidly converted to <sup>•</sup>OH under UV irradiation.<sup>2</sup> Therefore, it would be highly desirable if a low-power UV module was integrated into HEF systems. This combined strategy is expected to yield H<sub>2</sub>O<sub>2</sub>-free treatment solution while accelerating the mineralization of target

pollutants through the generation of additional <sup>•</sup>OH and the direct photolysis of photolabile intermediates.

Herein, a tandem system combining dual-cathode-based HEF and UV irradiation was developed for the first time, in an attempt to address the aforementioned challenges encountered in distributed EAOP treatment systems. For the dual-cathode HEF module, an air-diffusion cathode (ADC) with self-sustained aeration is employed for *in situ* electrosynthesis of H<sub>2</sub>O<sub>2</sub>, and a graphite felt catalytic cathode with high iron oxychloride loading (FeOCl/GF) is used for rapid conversion of H<sub>2</sub>O<sub>2</sub> into active species. These two cathodes perform their respective functions at different optimal working potentials to simultaneously achieve efficient H<sub>2</sub>O<sub>2</sub> production, Fe(III) electroreduction, and <sup>•</sup>OH formation. Of note is that the underutilized H<sub>2</sub>O<sub>2</sub> remaining in the HEF effluent will be continuously activated by the subsequently deployed UV irradiation module to eliminate the risk of oxidant residues and further improve the degradation efficiency. In addition, by constructing different independent/coupled systems (UV, H<sub>2</sub>O<sub>2</sub>, UV/H<sub>2</sub>O<sub>2</sub>, HEF, and HEF/UV), the reaction kinetics and H<sub>2</sub>O<sub>2</sub> concentration evolution corresponding to each isolated unit can be well discriminated. Thus, this study also enables the decoupling of the exact contribution of each subprocess and the elucidation of interesting antagonistic and synergistic phenomena that occurred in the dual-cathode HEF and UV tandem system.

## 2. Materials and methods

### 2.1. Electrode fabrication

A detailed description of the chemicals used is provided in Text S1.† ADC for *in situ* H<sub>2</sub>O<sub>2</sub> generation was prepared by a modified coating method.<sup>22</sup> Specifically, the pristine graphite felt (GF) was sequentially cleaned with ethanol and deionized water in an ultrasonic bath for 30 min, and then annealed at 400 °C for 4 h to remove impurities. The cleaned GF was soaked in the PTFE suspension (5 wt%) for 30 min and then taken out and dried at room temperature before use. Carbon black (CB) particles were ultrasonically dispersed in anhydrous ethanol for 10 min, followed by the dropwise addition of PTFE (at a CB-to-PTFE mass ratio of 5:3) and vigorous stirring at 70 °C until a wet paste was formed. The resulting paste was uniformly coated on one side of GF with a CB loading of 12.44 mg cm<sup>−2</sup>, and calcined at 350 °C for 60 min.

Considering that the catalytic cathode here is only responsible for the activation of ADC-produced H<sub>2</sub>O<sub>2</sub> but not for H<sub>2</sub>O<sub>2</sub> electrosynthesis, a FeOCl/GF composite with high FeOCl loading was fabricated in this study by improving our previously reported thermal-induced strategy.<sup>15</sup> In brief, the above pretreated GF was immersed in 5 mL FeCl<sub>3</sub>·6H<sub>2</sub>O ethanol solution with a concentration of 1.5 g mL<sup>−1</sup> for 3 h, and then evaporated and dried at 45 °C for 12 h to obtain the FeCl<sub>3</sub>/GF precursor. Afterwards, the precursor was transferred to a covered crucible and calcined at 220 °C for 1 h under atmospheric conditions with a temperature increase rate of 10 °C min<sup>−1</sup>, and

the resulting product was washed several times with deionized water to remove unreacted soluble iron salts. Note that in order to alleviate the shedding and leaching of active metals from the catalytic cathode during the degradation process, the FeOCl/GF composite was additionally subjected to a PTFE post-treatment process (*i.e.*, soaking in 1 wt% PTFE suspension followed by calcination at 180 °C). This not only improves the adhesion between FeOCl and the GF matrix, but also slows down the corrosive dissolution of the solid metal by the electrolyte due to the slight hydrophobic evolution at the solid-liquid interface.<sup>9</sup> A detailed description of the characterization methods used for different cathodes is presented in Text S2.†

## 2.2. Electrolyzer and degradation system

The electrolysis experiments involved in this work were all carried out in a custom-designed undivided reactor with a cylindrical cavity (Fig. 1). The ADC was embedded on the side wall of the reactor near the water inlet allowing one side of the cathode to be exposed to the air, while the FeOCl/GF catalytic cathode was placed inside the cavity for sufficient interaction with the upstream H<sub>2</sub>O<sub>2</sub> solution. Two Ti/Pt mesh electrodes were used as anodes and placed in parallel with the corresponding cathodes with an inter-electrode gap of 1.5 cm. All electrodes have an active area of 7.1 cm<sup>2</sup> (3 cm in diameter) unless otherwise specified. Note that each electrode pair was independently provided with the optimal current (galvanostatic mode) by different DC power supplies.

Degradation experiments were carried out with oxytetracycline (OTC) as the model pollutant in a tandem system of a dual-cathode electrolyzer and a pipeline type sterilizer equipped with a 6 W UV lamp (emission at 254 nm). A total volume of 300 mL of OTC aqueous solution (20 mg L<sup>-1</sup>) containing 50 mM Na<sub>2</sub>SO<sub>4</sub> was used as the simulated wastewater and supporting electrolyte in the feed reservoir, with its initial pH adjusted using 1 M of H<sub>2</sub>SO<sub>4</sub> or NaOH. Typical water treat-

ment processes were performed in a continuous recirculation mode. Driven by the peristaltic pump (Longer), the sewage containing OTC first enters the electrolysis unit and the rapid accumulation of H<sub>2</sub>O<sub>2</sub> occurs when it comes in contact with the ADC. The solution will then be forced to flow through the FeOCl/GF catalytic cathode during which considerable reactive radicals will be generated due to the activation of H<sub>2</sub>O<sub>2</sub> by the iron active center. Finally, the effluent from the electrolysis unit will enter the UV lamp module to completely consume the residual H<sub>2</sub>O<sub>2</sub> and further mineralize pollutants and intermediate molecules. In order to decouple the respective contributions of different subprocesses in the system, five different standalone or coupled systems, including UV (only UV irradiation unit, Fig. S1†), H<sub>2</sub>O<sub>2</sub> (electrolytic unit with ADC only, Fig. 1a), UV/H<sub>2</sub>O<sub>2</sub> (ADC + UV irradiation, Fig. 1b), HEF (electrolysis unit with dual cathodes, Fig. 1c), and HEF/UV (dual cathode + UV irradiation, Fig. 1d), were purposely constructed. H<sub>2</sub>O<sub>2</sub> accumulation over time was also performed in these settings, in the absence of pollutants.

## 2.3. Analytical methods

The concentrations of H<sub>2</sub>O<sub>2</sub> and total Fe in the solution were measured with a UV-vis spectrophotometer (UV-1100, Shanghai Mapada Instruments Co. Ltd, China) by the potassium titanium(IV) oxalate method at 400 nm and the 1,10-phenanthroline method at 510 nm, respectively. The current efficiency (CE) and electric energy consumption (EEC, kW h kg<sup>-1</sup>) for H<sub>2</sub>O<sub>2</sub> electrosynthesis were calculated by the following two equations:

$$CE = \frac{nFCV}{It} \times 100\% \quad (1)$$

where  $n$  is the number of electrons transferred for O<sub>2</sub> reduction to H<sub>2</sub>O<sub>2</sub> ( $n = 2$ ),  $F$  is the Faraday constant (96 486 C mol<sup>-1</sup>),  $C$  is the concentration of H<sub>2</sub>O<sub>2</sub> (mol L<sup>-1</sup>),  $V$  is the volume of the

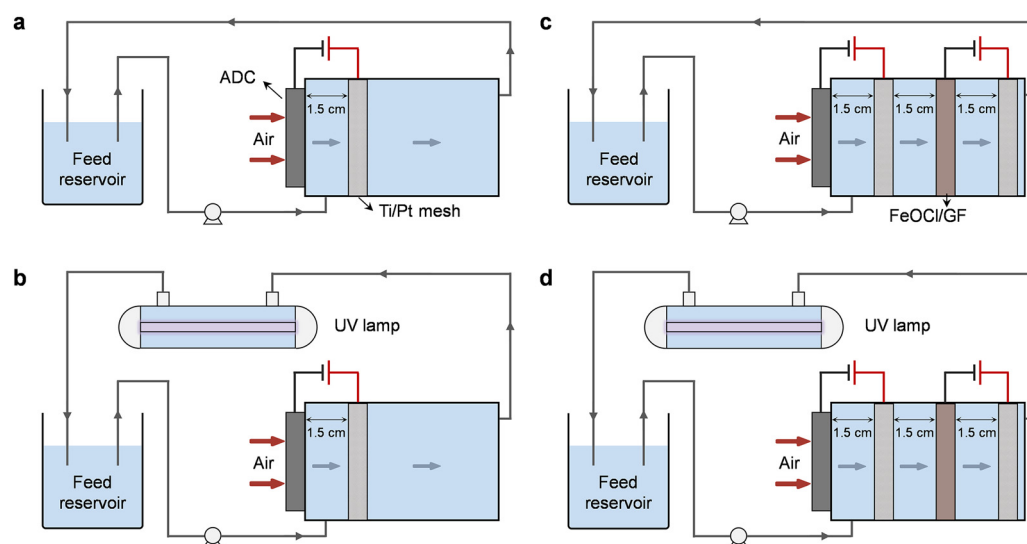


Fig. 1 Schematic illustration of different standalone or coupled degradation systems: (a) H<sub>2</sub>O<sub>2</sub>, (b) UV/H<sub>2</sub>O<sub>2</sub>, (c) HEF, and (d) HEF/UV.

electrolyte (L),  $I$  is the current (A), and  $t$  is the electrolysis time (s).

$$\text{EEC} = \frac{1000UIt}{CV} \quad (2)$$

where  $U$  is the average cell voltage (absolute value, V),  $t$  is the electrolysis time (h), and  $C$  is the concentration of  $\text{H}_2\text{O}_2$  ( $\text{mg L}^{-1}$ ).

The evolution of the OTC concentration was monitored using the same spectrophotometer at 357 nm. Prior to performing the analyses, the collected samples were filtered using a  $0.22 \mu\text{m}$  filter. The OTC degradation kinetics for different systems were determined using a pseudo-first-order model as described in eqn (3):

$$\ln\left(\frac{C_t}{C_0}\right) = -kt \quad (3)$$

where,  $k$  is the apparent pseudo-first-order rate constant;  $C_0$  and  $C_t$  are the OTC concentrations at the initial time and following electrolysis for time  $t$ , respectively.

The concept of synergistic factor (sf) was introduced herein to characterize the antagonistic and synergistic effects occurring in the dual-cathode HEF-coupled UV radiation system, and was calculated as follows:

$$\text{sf} = \frac{k_{\text{HEF/UV}}}{k_{\text{HEF}} + k_{\text{UV/H}_2\text{O}_2}} \quad (4)$$

where  $k_{\text{HEF/UV}}$ ,  $k_{\text{HEF}}$ , and  $k_{\text{UV/H}_2\text{O}_2}$  represent the rate constants of the HEF/UV system, HEF system, and UV/ $\text{H}_2\text{O}_2$  system, respectively.

The OTC mineralization rate was monitored by a total organic carbon (TOC) analyzer (TOC-L, Shimadzu, Japan). The oxidation by-products of OTC were identified by ultrahigh performance liquid chromatography coupled with a mass spectrometry (LC-MS-8050, Shimadzu, Japan) system equipped with a C18 column ( $2.1 \text{ mm} \times 100 \text{ mm}$ ,  $1.7 \mu\text{m}$ ), and the detailed measurement method is given in our previous work.<sup>15</sup> Ecological Structure–Activity Relationship (ECOSAR) software was utilized to predict the acute and chronic toxicity of OTC and its degradation intermediates. The active species generation in the system was identified by electron paramagnetic resonance (EPR) spectroscopy (Micro-EPR, Bruker). DMPO was applied as the spin-tapping agents for  $\cdot\text{OH}$ ,  $\cdot\text{O}_2^-$  (methanol system), and  $\text{SO}_4^{\cdot-}$ . TEMP was used to detect  $^1\text{O}_2$ .

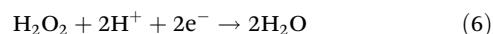
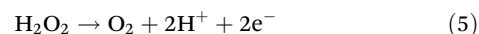
### 3. Results and discussion

#### 3.1. Characterization and electrocatalytic performance of different cathodes

Scanning electron microscopy (SEM) images reveal that the prepared ADC is characterized by a double-layer structure with PTFE-treated GF as the diffusion layer and CB as the catalytic layer (Fig. S2†). The high macroporosity of the GF layer allows the free mass transfer of  $\text{O}_2$  from the atmosphere to the reaction boundary, while the strong hydrophobicity of the CB layer (contact angle of  $136.1^\circ$  in the inset of Fig. S2†) ensures unim-

peded  $\text{O}_2$  capture at the three-phase interface. Therefore, this electrode configuration can endow the  $\text{H}_2\text{O}_2$  production process with an interesting self-sustained aeration characteristic driven by a hydrophobicity-controlled  $\text{O}_2$  concentration gradient between the reaction interface and the atmosphere. As a result, the significant energy consumption (even exceeding 50% of the total cost) associated with aeration facilities in conventional submerged or gas diffusion electrode systems is effectively avoided.<sup>15,22</sup>

The  $\text{H}_2\text{O}_2$  production performance of ADC was then evaluated (Fig. 2a). Obviously, the accumulation of  $\text{H}_2\text{O}_2$  increased linearly with the reaction time for different current densities ( $5\text{--}100 \text{ mA cm}^{-2}$ ). And the final  $\text{H}_2\text{O}_2$  concentration corresponding to each measurement (60 min) was also observed to increase linearly with the applied current density ( $R^2 = 0.995$ , inset in Fig. 2c), with a maximum of  $1261.9 \text{ mg L}^{-1}$  at  $100 \text{ mA cm}^{-2}$ . This indicated that the  $2\text{e}^-$  ORR process was no longer limited by the  $\text{O}_2$  mass transfer but only controlled by the electron transfer within the scope of the investigation. Generally, CE and EEC were considered as the key parameters to determine the economic viability of an electrochemical system applied toward  $\text{H}_2\text{O}_2$  production.<sup>4</sup> As revealed in Fig. 2b, although the increase in the current density yielded a decrease in CE (from 104.9% at  $5 \text{ mA cm}^{-2}$  to 85.3% at  $100 \text{ mA cm}^{-2}$ ), the performance is still satisfactory because CE is always higher than 85% or even higher than 90% in the range of current density less than  $45 \text{ mA cm}^{-2}$ . The CE exceeding the theoretical maximum value at  $5 \text{ mA cm}^{-2}$  may be due to the amplification of small sampling errors by the CE calculation method (eqn (1)). And the observed decrease in CE at higher current densities can be ascribed to the promotion of parasitic reactions involving either  $\text{H}_2\text{O}_2$  decomposition (*via* anodic oxidation and cathodic reduction) or the hydrogen evolution reaction (eqn (5)–(7)). For EEC (Fig. 2c), in contrast, it exhibited a positive correlation with the applied current density due to the increased cell voltage. Nevertheless, the EEC of the ADC system at  $5 \text{ mA cm}^{-2}$  ( $5.3 \text{ kW h kg}^{-1}$ ) was noted to be very competitive with that of previously reported  $\text{H}_2\text{O}_2$  electrosynthesis processes ( $3.7\text{--}53.9 \text{ kW h kg}^{-1}$ , Table S1†). Furthermore, although the application of a current density of  $100 \text{ mA cm}^{-2}$  ( $44.2 \text{ kW h kg}^{-1}$ ) resulted in an 8.3-fold increase in EEC over the value at  $5 \text{ mA cm}^{-2}$  ( $5.3 \text{ kW h kg}^{-1}$ ), the corresponding  $\text{H}_2\text{O}_2$  production ( $1261.9 \text{ mg L}^{-1}$ ) was 16.2-fold higher than that at  $5 \text{ mA cm}^{-2}$  ( $77.7 \text{ mg L}^{-1}$ ). Therefore, ADC with cheap and easy preparation is highly desirable for the subsequent HEF process, due to its stable  $\text{H}_2\text{O}_2$  supply and excellent process efficiency with respect to both yield and energy consumption.



The physicochemical properties of the catalytic cathode were also characterized by different techniques. The diffraction



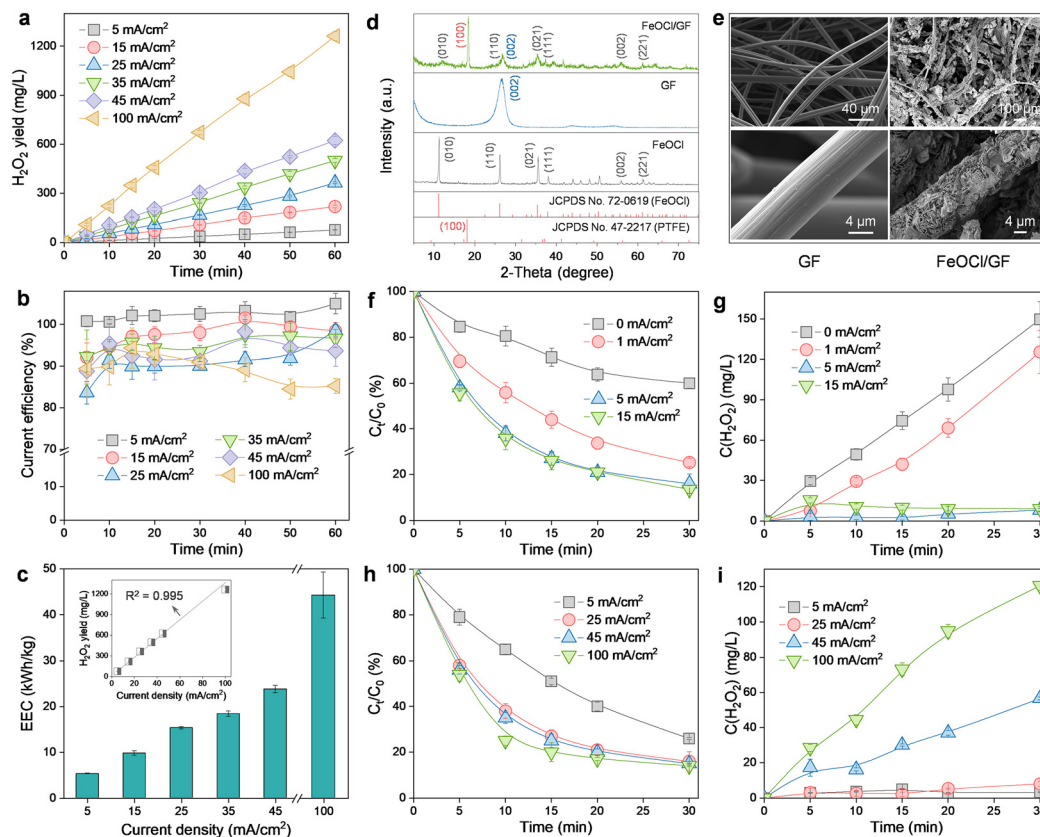


**Fig. 2** Physicochemical properties and catalytic performance of different cathodes. Effect of current density on the (a) yield, (b) current efficiency, and (c) energy consumption of the  $\text{H}_2\text{O}_2$  production at ADC; (d) XRD patterns of FeOCl, GF, and FeOCl/GF; and (e) SEM images of GF and FeOCl/GF; effect of current density on the OTC degradation performance of the dual-cathode HEF system and the corresponding  $\text{H}_2\text{O}_2$  concentration evolution (conditions:  $[\text{OTC}] = 20 \text{ mg L}^{-1}$  and  $\text{pH} = 4$ ): (f) and (g) FeOCl/GF, (h) and (i) ADC.

peaks related to GF ((002))<sup>9</sup> and FeOCl ((010), (110), (021), (111), (002), and (221))<sup>23</sup> were observed in the X-ray diffractometer (XRD) pattern of FeOCl/GF (Fig. 2d), indicating the successful formation of the composite. Note that the diffraction peak corresponding to the (010) plane of FeOCl in the FeOCl/GF composite was found to be shifted to higher angles compared to the FeOCl sample, which may be attributed to the interaction between the metal and the carbon substrate that induces narrowing of the interlayer spacing of FeOCl through structural modulation. According to the low-magnification SEM images, pristine GF presents a porous network structure composed of carbon fibers with smooth surfaces, while FeOCl/GF fibers reveal a rather rough surface morphology (Fig. 2e). High-magnification SEM images confirm that the rough transition on the carbon fiber surface is caused by the omnidirectional coverage of sheet-like FeOCl. In previously reported single-cathode HEF systems, the fine-tuning of the solid catalyst growth process on the surface of the catalytic cathode, although challenging, is necessary and mandatory to simultaneously expose carbon and metal sites for the realization of the intended bifunctionality (*i.e.*, sequential  $2\text{e}^-$  ORR and Fenton activation).<sup>6</sup> However, the catalytic cathode in the present work only exhibits activation function for  $\text{H}_2\text{O}_2$ , which

allows high loading of FeOCl on GF to thoroughly stimulate the catalytic potential of the composite cathode. The brighter colors corresponding to Fe, O, and Cl elements compared to the C element in the energy dispersive spectroscopy (EDS) results strongly demonstrate the rather high FeOCl loading of the synthesized FeOCl/GF composite cathode (Fig. S3†). In addition, a PTFE post-treatment process was also performed on this catalytic cathode to alleviate the risk of catalyst shedding and leaching exacerbated by high loading, relying on the bonding and hydrophobic protection effects of PTFE.<sup>9</sup> A characteristic peak indexed to the (100) plane of PTFE was observed in the XRD pattern of the FeOCl/GF composite, suggesting the successful functionalization of PTFE.<sup>9</sup>

The efficacy of the FeOCl/GF catalytic cathode was then investigated by fixing the current density applied to the ADC at  $25 \text{ mA cm}^{-2}$ . It can be found that the degradation of OTC is limited when the FeOCl/GF cathode was not supplied with current (Fig. 2f). This may be because the collision probability of the catalyst and  $\text{H}_2\text{O}_2$  in this filter configuration is much lower than that of the typical HEF process with the catalyst suspended. More importantly, the integrated catalysts of the composite cathode are always exposed to the strong oxidizing microenvironment (aggressive reactive oxygen species),

leading to the rapid depletion of low-valent active Fe(II) and the passivation of the catalytic cathode.<sup>13</sup> This can be confirmed by the concentration evolution of H<sub>2</sub>O<sub>2</sub>, as the accumulated concentration of H<sub>2</sub>O<sub>2</sub> in the dual-cathode system with no current applied to the FeOCl/GF cathode is only slightly lower than that in the ADC single-cathode system (Fig. S4†). Interestingly, the OTC degradation kinetics were accelerated once a constant current was applied to the catalytic cathode, indicating a significant improvement in the activation of the catalytic cathode to H<sub>2</sub>O<sub>2</sub>. This is indeed the case as demonstrated in Fig. 2g that the accumulated concentration of H<sub>2</sub>O<sub>2</sub> decreased rapidly as the current was applied, and even almost no residual H<sub>2</sub>O<sub>2</sub> was detected when the catalytic cathode was operated with a current density higher than 5 mA cm<sup>-2</sup>. In this work, the Fe(II)/Fe(III) redox cycling on the surface of the composite cathode can be kept quasi-reversible with the assistance of an electric field (as evidenced by the relative Fe(II) content on the FeOCl/GF cathode surface increasing from 46.4% before the reaction to 47.3% after the reaction, Fig. S5†),<sup>13,24</sup> which accelerates catalytic activation of ADC-produced H<sub>2</sub>O<sub>2</sub> and thus the degradation of OTC. However, a further increase in the current density will lead to a decrease in the Fe(III) reduction. This can be explained by the promotion of side reactions, like the hydrogen evolution reaction, which not only competed with the electroreduction of Fe(III), but more seriously, caused the hydrolysis of active iron to inert hydrous oxyhydroxides due to the local alkalization near the catalyst.<sup>16</sup> For this reason, as the current density applied to the FeOCl/GF cathode increased up to 15 mA cm<sup>-2</sup>, the OTC degradation efficiency did not change significantly compared to 5 mA cm<sup>-2</sup> (Fig. 2f). Note that the above discussions all exclude Fe homogeneous oxidation contributions because the concentration of total Fe leached from the catalytic cathode is too low (1.4 mg L<sup>-1</sup> vs. 68.0 mg L<sup>-1</sup> for FeOCl/GF without PTFE post-treatment, Fig. S6†) to drive significant degradation of OTC (Fig. S7†).

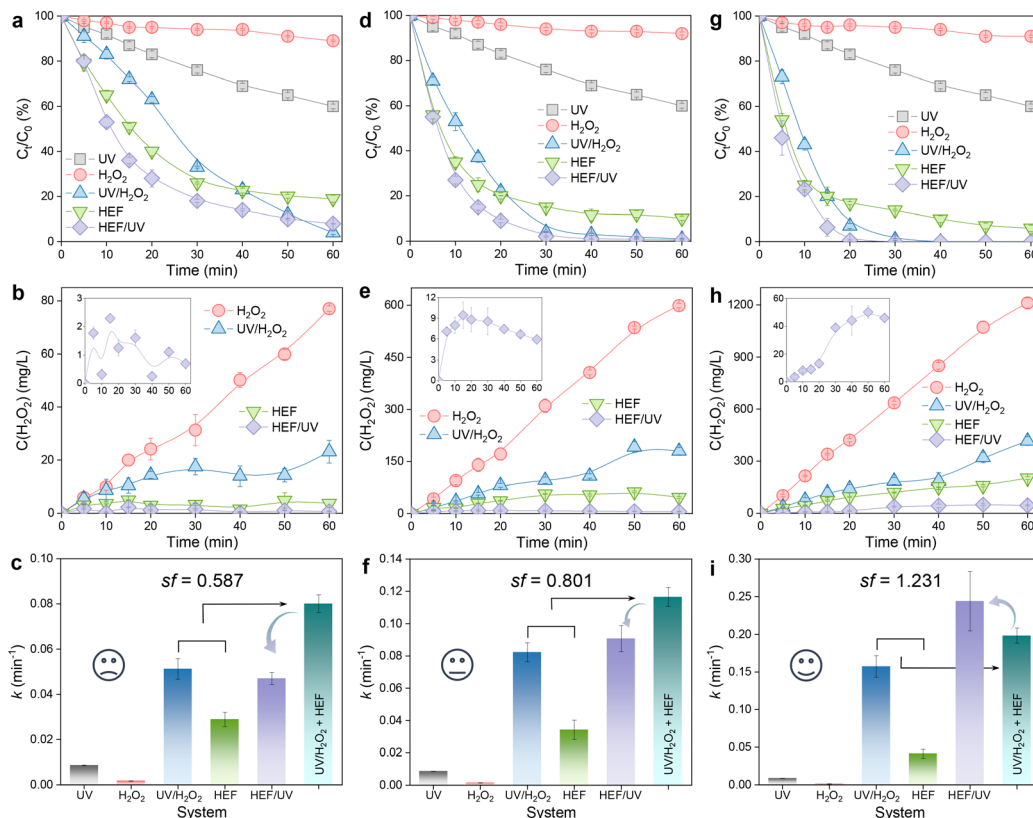
The effect of the ADC on the reactivity of the dual-cathode HEF was also investigated by fixing the operating current density of the catalytic cathode at 5 mA cm<sup>-2</sup> (Fig. 2h). For comparison with the conventional single-cathode HEF process, the current density applied to the ADC was adjusted to the same 5 mA cm<sup>-2</sup> as the catalytic cathode. A reduced OTC degradation rate was observed compared with a current density of 25 mA cm<sup>-2</sup>, which may be attributed to the fact that the concentration of H<sub>2</sub>O<sub>2</sub> produced by the ADC was too low to keep up with the demand of the FeOCl/GF cathode. This is well supported by the evolution of the H<sub>2</sub>O<sub>2</sub> concentration in Fig. 2i, with almost no H<sub>2</sub>O<sub>2</sub> accumulation for ADC current densities in the range of 5 to 25 mA cm<sup>-2</sup>. It has been recently reported that a single-cathode HEF system based on the same FeOCl/GF catalytic cathode can afford a degradation rate constant (*k* value) of 0.05629 min<sup>-1</sup> for 100 mL of OTC solution (10 mg L<sup>-1</sup>) at 5 mA cm<sup>-2</sup>,<sup>15</sup> while the *k* value of the present dual-cathode HEF system was established to be 0.04505 min<sup>-1</sup> (Fig. S8†) for 300 mL of OTC solution (20 mg L<sup>-1</sup>) under the same operating conditions (*i.e.*, 5 mA cm<sup>-2</sup> for

both ADC and FeOCl/GF cathodes). By comparing these results, one can conclude that the dual-cathode HEF system developed herein was highly competitive as it allowed a 6-fold higher total pollutant treatment (6 mg vs. 1 mg) with only a 1.2-fold lower *k* value (0.04505 min<sup>-1</sup> vs. 0.05629 min<sup>-1</sup>) compared to the single-cathode HEF system. Therefore, this study demonstrated that the separation of the composite cathode-based HEF process into independent H<sub>2</sub>O<sub>2</sub> production and activation processes may be highly desirable as it enabled the two individual subprocesses to be performed optimally. Of course, attention must be paid to the additional electricity cost consumed by the FeOCl/GF electrode pair, and rational system optimization to improve the economics of the dual-cathode HEF process, which is necessary for future research. It is also worth noting that increasing the working current density of the ADC can further accelerate the degradation of OTC, but at the expense of excessive H<sub>2</sub>O<sub>2</sub> residue in the effluent (especially >100 mg L<sup>-1</sup> at 100 mA cm<sup>-2</sup>). This trade-off can be overcome by adding a UV radiation module after the dual-cathode HEF process, which will be discussed in detail in the next section.

### 3.2. Process efficiency of the dual-cathode HEF and UV tandem system

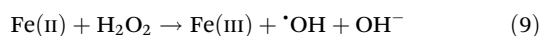
A matter scarcely addressed in previous HEF processes based on *in situ* H<sub>2</sub>O<sub>2</sub> electrosynthesis is the examination of the residual H<sub>2</sub>O<sub>2</sub> concentration. Most reports have been confined solely to the analysis of pollutant removal, without considering the fate of unreacted H<sub>2</sub>O<sub>2</sub> remaining in the bulk solution after treatment. The idea of the present study is to integrate a low-power UV module at the outlet of the dual-cathode HEF facility to eliminate the risk of the H<sub>2</sub>O<sub>2</sub> residue. In addition, the purpose of the following experiments also involves evaluating the efficacy of the coupled process by comparing OTC degradation and H<sub>2</sub>O<sub>2</sub> concentration evolution achieved by different configurations (*i.e.*, UV, H<sub>2</sub>O<sub>2</sub>, UV/H<sub>2</sub>O<sub>2</sub>, HEF, and HEF/UV). Experiments were carried out by fixing the optimum current density of the FeOCl/GF catalytic cathode at 5 mA cm<sup>-2</sup> (as demonstrated in section 3.1) but varying the current density of the ADC (5–100 mA cm<sup>-2</sup>).

Fig. 3 shows the decay of the OTC concentration over time in different systems and the corresponding H<sub>2</sub>O<sub>2</sub> concentration evolution. Regardless of the current density applied on the ADC, H<sub>2</sub>O<sub>2</sub> alone can hardly oxidize OTC with almost negligible *k* values due to its weak oxidizing ability (Fig. 3a, d, and g). This is evidenced by the insignificant difference in the accumulation of H<sub>2</sub>O<sub>2</sub> using the same ADC in the presence of pollutants (Fig. 3b, e, and h) *versus* the absence of pollutants (Fig. 2a). Although OTC can be degraded by direct photolysis in the UV system, its efficiency is still limited and unsatisfactory (Fig. 3a, d, and g). After incorporating UV radiation and/or FeOCl/GF catalytic cathode into the H<sub>2</sub>O<sub>2</sub> system (*i.e.*, HEF/UV, UV/H<sub>2</sub>O<sub>2</sub>, and HEF), the concentration of OTC decreased significantly due to the production of oxidant species homogeneously in the bulk solution (photolytic homolysis of H<sub>2</sub>O<sub>2</sub> by UV radiation, eqn (8))<sup>25</sup> and/or heterogeneously at the surface



**Fig. 3** Investigation of the reaction characteristics of each sub-process in the tandem system. Effect of different ADC operating current densities on process efficiency: (a–c) 5 mA cm<sup>-2</sup>, (d–f) 45 mA cm<sup>-2</sup>, and (g–i) 100 mA cm<sup>-2</sup>. OTC degradation performance in different systems (first row), corresponding H<sub>2</sub>O<sub>2</sub> concentration evolution (second row), and comparison of apparent rate constant *k* (third row) (conditions: [OTC] = 20 mg L<sup>-1</sup>, pH = 4, *I*<sub>FeOCl/GF</sub> = 5 mA cm<sup>-2</sup>, and UV = 6 W).

of the catalytic cathode (Fenton activation of H<sub>2</sub>O<sub>2</sub> by FeOCl/GF, eqn (9)). These phenomena were consistent with the greatly attenuated H<sub>2</sub>O<sub>2</sub> accumulation in HEF/UV, UV/H<sub>2</sub>O<sub>2</sub>, and HEF systems compared with the H<sub>2</sub>O<sub>2</sub> standalone system in Fig. 3b, e, and h. Furthermore, it is worth noting that the H<sub>2</sub>O<sub>2</sub> consumption rate of the HEF/UV tandem system was found to be close to 100% for all operating current densities of the ADC, since there was almost no H<sub>2</sub>O<sub>2</sub> residue in the treated solution. For the UV/H<sub>2</sub>O<sub>2</sub> and HEF systems, however, a relatively high percentage of H<sub>2</sub>O<sub>2</sub> (especially 36.4% (416.4 mg L<sup>-1</sup>) for UV/H<sub>2</sub>O<sub>2</sub> and 16.7% (201.8 mg L<sup>-1</sup>) for HEF at 100 mA cm<sup>-2</sup>) did not participate in the treatment process after 60 min of reaction. These results suggest that the technology proposed in this study is highly efficient for further improving the oxidation capacity of the dual-cathode HEF process without generating H<sub>2</sub>O<sub>2</sub>-containing effluent.

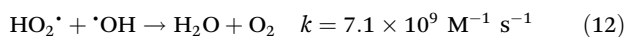
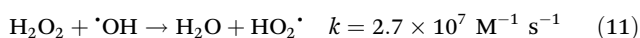
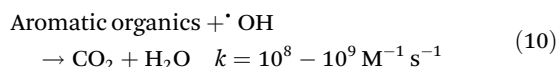


In addition, the reaction kinetics of different independent or coupled processes were carefully analyzed, and accordingly the *sf* values at different operating current densities were obtained. Interestingly, as presented in Fig. 3c, f, and i, the *sf*

value of the tandem system increases with the current density applied to the ADC and is >1 at 100 mA cm<sup>-2</sup>. This means that the *k* value corresponding to the HEF/UV configuration is higher than the sum of the individual HEF and UV/H<sub>2</sub>O<sub>2</sub> processes, indicating that the tandem of dual-cathode HEF and UV radiation within the same system leads to synergistic acceleration of OTC degradation. Whereas when the current density is less than 100 mA cm<sup>-2</sup>, the *sf* value <1 suggests that there seems to be some unfavorable interaction between HEF and UV in the tandem system. Therefore, the following discussion will emphasize the differences in the reaction characteristics at different current densities to gain mechanistic insights into the electrooxidation process of the HEF/UV tandem system.

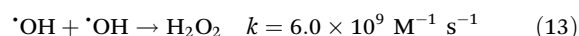
At 5 mA cm<sup>-2</sup>, the OTC degradation in the dual-cathode HEF and UV tandem systems was faster than the HEF or UV/H<sub>2</sub>O<sub>2</sub> standalone systems before 50 min (Fig. 3a), due to the additional free radicals generated by UV decomposition of the residual trace H<sub>2</sub>O<sub>2</sub> (3.7 mg L<sup>-1</sup>, Fig. 3b) in the HEF effluent. After 50 min, however, the degradation rate of OTC gradually slowed down and was even worse than that of the UV/H<sub>2</sub>O<sub>2</sub> system, which resulted in the *k* value of the tandem system being lower than that of the UV/H<sub>2</sub>O<sub>2</sub> standalone system (Fig. 3c). Therefore, the *sf* value at a current density of 5 mA cm<sup>-2</sup> cannot be greater than 1, according to the calculation

principle (eqn (4)). Regarding the extremely low *sf* value (0.587) under these conditions, it can be explained by the following two aspects. For one thing, the residual concentration of H<sub>2</sub>O<sub>2</sub> in the solution after HEF treatment in the tandem system was too low to fully exert the efficiency of the subsequent UV/H<sub>2</sub>O<sub>2</sub> system. The similar OTC degradation trends of the HEF standalone system and HEF/UV system also indicated that the HEF subprocess in the coupled process mainly contributed to OTC degradation under these conditions. For another, the UV/H<sub>2</sub>O<sub>2</sub> system achieved a higher OTC degradation rate (0.05126 min<sup>-1</sup> vs. 0.02885 min<sup>-1</sup>, Fig. 3c) with less H<sub>2</sub>O<sub>2</sub> consumption (69.9% vs. 95.1%, Fig. 3b) compared to the HEF system, implying the ineffective decomposition of H<sub>2</sub>O<sub>2</sub> in the HEF module. This is evidenced by the fact that FeOCl/GF cathode always exhibited a significantly faster H<sub>2</sub>O<sub>2</sub> decomposition rate than the UV lamp at different initial concentrations of H<sub>2</sub>O<sub>2</sub> (Fig. S9†). According to the well-established reaction pathways in the literature,<sup>5</sup> there is actually a competition between different species in the influent (pollutant molecules and H<sub>2</sub>O<sub>2</sub>) for the reaction with <sup>•</sup>OH generated heterogeneously on the FeOCl/GF surface (eqn (10)–(12)).<sup>7</sup> The relatively high concentration of OTC in the early stage of the reaction makes the degradation reaction between pollutant molecules and free radicals (mainly <sup>•</sup>OH) in the system dominate. However, as the OTC concentration decays to a critical value (at 50 min), the quenching reaction between H<sub>2</sub>O<sub>2</sub> in the flowing solution and the locally high concentration of surface <sup>•</sup>OH at the FeOCl/GF catalytic cathode instead dominates, which in turn deteriorates the OTC degradation efficiency. A similar phenomenon to the wasting reaction between H<sub>2</sub>O<sub>2</sub> and <sup>•</sup>OH affects the treatment performance of EAOPs was also observed by Sánchez-Montes *et al.*<sup>19</sup> and Dong *et al.*<sup>26</sup> Therefore, it can be concluded that the low *sf* value at 5 mA cm<sup>-2</sup> is mainly attributed to the wasting reaction of reactive oxygen species inherent in the dual-cathode HEF process, which cannot be mitigated after the introduction of the UV module.



Different from 5 mA cm<sup>-2</sup>, the OTC degradation of the HEF/UV system at 45 mA cm<sup>-2</sup> was significantly faster than each standalone system throughout the entire reaction period (Fig. 3d), and the corresponding *k* value was also higher than each standalone system (Fig. 3f). This is because the residual H<sub>2</sub>O<sub>2</sub> concentration in the effluent from the HEF unit at 45 mA cm<sup>-2</sup> exceeds 11 times that at 5 mA cm<sup>-2</sup> (47.1 mg L<sup>-1</sup> vs. 3.7 mg L<sup>-1</sup>), which allows more homogeneous <sup>•</sup>OH to be generated in the subsequent UV module for oxidative degradation. Nevertheless, the *sf* value under these conditions was noticed to be still less than 1 (0.801), indicating that the self-scavenging reaction between H<sub>2</sub>O<sub>2</sub> and heterogeneous <sup>•</sup>OH on the

surface of the catalytic cathode still occurred. This can be confirmed by the decrease of H<sub>2</sub>O<sub>2</sub> concentration after 20 min of reaction in the HEF/UV system (inset of Fig. 3e). Encouragingly, the *sf* value was greater than 1 upon increasing the current density of the ADC to 100 mA cm<sup>-2</sup> (Fig. 3i). According to the kinetic constant information of the EF chain reaction established by Brillas *et al.*,<sup>7</sup> the rate constant of the <sup>•</sup>OH recombination reaction (eqn (13)) was determined to be two orders of magnitude higher than that of the aforementioned self-scavenging reaction (eqn (11)). Based on this, it could be speculated that due to the further increase in the relative content of homogeneous <sup>•</sup>OH in the UV unit (by activating a higher concentration of residual H<sub>2</sub>O<sub>2</sub> in the HEF effluent at 100 mA cm<sup>-2</sup>, Fig. 3h), the dimerization reaction between these homogeneous <sup>•</sup>OH and heterogeneous <sup>•</sup>OH generated at the FeOCl/GF cathode might be promoted, thereby decreasing the wasting reaction of H<sub>2</sub>O<sub>2</sub> with heterogeneous <sup>•</sup>OH. More importantly, H<sub>2</sub>O<sub>2</sub>, the dimerization product of homogeneous <sup>•</sup>OH and heterogeneous <sup>•</sup>OH, would flow back into the UV irradiation module with higher H<sub>2</sub>O<sub>2</sub> activation efficiency and be converted into <sup>•</sup>OH again to participate in the OTC degradation process. The gradual increase of the accumulated concentration of H<sub>2</sub>O<sub>2</sub> in the HEF/UV system (inset of Fig. 3h) can also support the above speculation, which is completely different from the situations of 5 and 45 mA cm<sup>-2</sup> (inset of Fig. 3b and e). Note that the faster accumulation of H<sub>2</sub>O<sub>2</sub> after 20 min may be related to the conversion of the dominant reaction in the system from the degradation reaction between pollutant molecules and <sup>•</sup>OH to the dimerization reaction between <sup>•</sup>OH (since OTC has been completely degraded at 20 min, Fig. 3g).



Additionally, this interesting synergistic effect between dual-cathode HEF and UV was noted independent of the initial pH of the treatment solution. As illustrated in Fig. S10,† under the optimal working current density justified above (*i.e.*, 5 mA cm<sup>-2</sup> for FeOCl/GF and 100 mA cm<sup>-2</sup> for ADC), the pH range was set from 4 to 8 to investigate the influence of initial pH on the oxidation capacity of the HEF/UV tandem system. Similar to the results at pH 4, the OTC degradation efficiency of the HEF/UV tandem system at pH 6 and 8 was significantly superior to that of various isolated systems, and the *sf* values at pH 6 (1.515) and 8 (1.467) were both greater than 1 and higher than that at pH 4 (1.231). This can be because the increased residual H<sub>2</sub>O<sub>2</sub> in the HEF effluent at pH 6 and 8 would promote the generation of homogeneous <sup>•</sup>OH in the UV module, thus further weakening the wasting reaction (Fig. S10b, e, and h†). Notably, the highest *sf* (1.515) and *k* (0.2978 min<sup>-1</sup>) values corresponding to the HEF/UV tandem system were achieved at a solution pH of 6, which was considered to be a compromise between the different reaction characteristics of each subprocess in terms of initial solution pH (see the discussion shown in Fig. S10 and S11† for detailed reasons). This finding indicates that the HEF/UV tandem

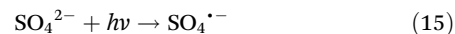
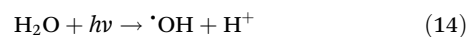


system is of great practical value since the majority of the effluents from industrial companies are at circumneutral pH.

### 3.3. Identification of reactive oxygen species responsible for OTC removal

The above discussion on the removal of OTC was based on the radical pathway dominated by  $\cdot\text{OH}$ . However, an increasing number of recent studies have reported that in addition to  $\cdot\text{OH}$ , there may be other active species-controlled radical pathways, or even nonradical pathways, during EAOP treatment.<sup>17,27–29</sup> In view of this, EPR tests were implemented in different systems to determine the generated reactive oxygen species. When DMPO was used as a spin trapping agent (Fig. 4a), a weak quadruple peak signal for DMPO- $\cdot\text{OH}$  (intensity ratio 1 : 2 : 2 : 1) appeared in the UV system, which may be caused by the ionization of  $\text{H}_2\text{O}$  molecules by UV radiation (eqn (14)).<sup>30</sup> With the coupling of the ADC (*i.e.*, the UV/ $\text{H}_2\text{O}_2$  system), the photolytic activation of  $\text{H}_2\text{O}_2$  by UV radiation resulted in a significant increase in the peak intensity of the DMPO- $\cdot\text{OH}$  signal. A similar phenomenon in the HEF system can be attributed to the Fenton activation of  $\text{H}_2\text{O}_2$  at the  $\text{FeOCl}/\text{GF}$  catalytic cathode. The production of the highest concentration of  $\cdot\text{OH}$  was achieved in the HEF/UV tandem system due to the synergistic effect between these two subprocesses. Importantly, the signal intensity of DMPO- $\cdot\text{OH}$  did not change significantly as the reaction proceeded (5 min to 10 min), indicating that  $\cdot\text{OH}$  was continuously generated in this tandem system to compensate for the self-quenching effect caused by its short lifetime.<sup>31</sup> Note that the DMPO- $\text{SO}_4^{\cdot-}$  signal was also detected in those systems equipped with the UV module, although the signal intensity was generally weaker than that of

$\cdot\text{OH}$ . In a previous study of the photocatalytic oxidation reaction, Liu *et al.* proved that minor  $\text{SO}_4^{2-}$  ions can be directly excited to convert into  $\text{SO}_4^{\cdot-}$  under UV irradiation (eqn (15)).<sup>32</sup> This could also explain why no DMPO- $\text{SO}_4^{\cdot-}$  signal was observed in the HEF standalone system.



For the case using TEMP as the spin trapping agent (Fig. 4b), the 3-line TEMP- $^1\text{O}_2$  signal was detected in all systems except for HEF, with the order of peak intensity as follows: HEF/UV > UV/ $\text{H}_2\text{O}_2$  > UV. Regarding the generation path of  $^1\text{O}_2$ , although most previous studies emphasized that  $\cdot\text{O}_2^-$  as an intermediate is critical for the conversion of  $^1\text{O}_2$ ,<sup>33</sup> it may be trivial in our work. This was evidenced by the failure to detect the DMPO- $\cdot\text{O}_2^-$  signal in all systems (Fig. 4c). Similar to  $\text{SO}_4^{\cdot-}$ , the generation of  $^1\text{O}_2$  in the present system may also be closely related to UV radiation. When the solution flows through the UV lamp module, both dissolved oxygen and  $\cdot\text{OH}$  are likely to be excited and transformed into  $^1\text{O}_2$  (eqn (16) and (17)), as demonstrated by Jin *et al.*<sup>34</sup> and Guo *et al.*<sup>27</sup> Accordingly, the observed stronger TEMP- $^1\text{O}_2$  signals in the UV/ $\text{H}_2\text{O}_2$  and HEF/UV systems compared to the UV standalone system could be interpreted as the elevated concentration of homogeneous  $\cdot\text{OH}$ , and the additional dissolved oxygen contributed by the anodic oxygen evolution reaction during electrolysis, respectively. Note, however, that the concentration of  $^1\text{O}_2$  in the HEF/UV system was found to gradually decrease (Fig. 4b) and remained stable after 20 min (Fig. S12†), due to

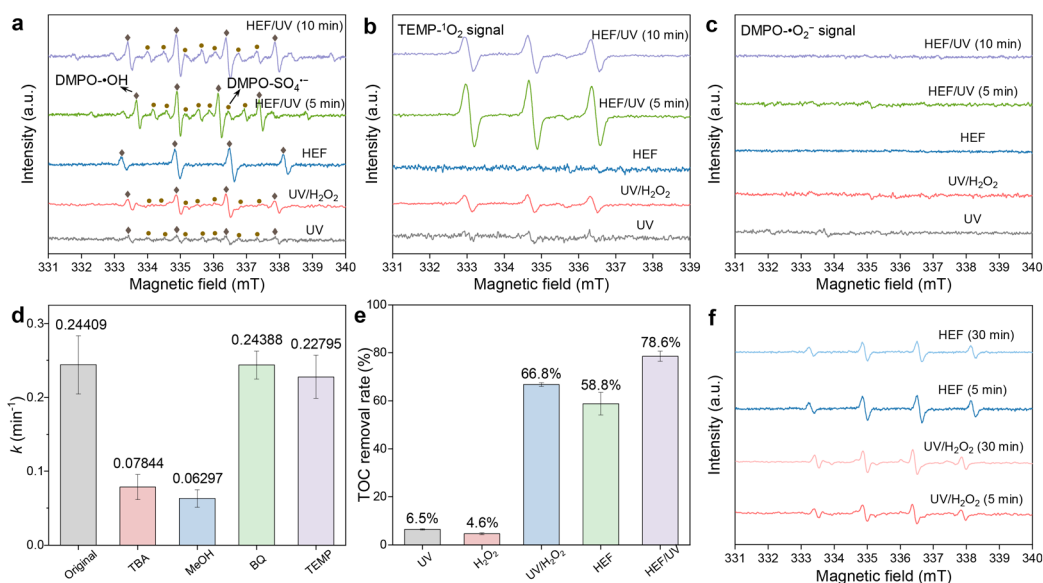
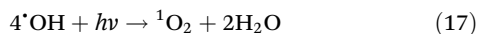


**Fig. 4** Identification of active species formed in the tandem system. EPR spectra of (a) DMPO- $\cdot\text{OH}$  (DMPO- $\text{SO}_4^{\cdot-}$ ), (b) TEMP- $^1\text{O}_2$ , and (c) DMPO- $\cdot\text{O}_2^-$  in different systems (conditions: [DMPO] = 200 mM, [TEMP] = 25 mM, pH = 4,  $I_{\text{ADC}}$  = 100 mA cm $^{-2}$ ,  $I_{\text{FeOCl/GF}}$  = 5 mA cm $^{-2}$ , and UV = 6 W); (d) effects of TBA (200 mM), MeOH (200 mM), BQ (5 mM), and TEMP (2.5 mM) on OTC degradation kinetics in HEF/UV tandem systems; (e) TOC removal rate of different systems; and (f) EPR spectra of DMPO- $\cdot\text{OH}$  in the UV/ $\text{H}_2\text{O}_2$  and HEF systems at different reaction times.

the consumption of dissolved oxygen at the ADC and FeOCl/GF cathode *via* the ORR.



In order to distinguish the relative contributions of the abovementioned different reactive oxygen species in the OTC degradation process, chemical quenching experiments were also performed with the HEF/UV system as a representative. As shown in Fig. 4d, TBA, BQ, and TEMP were chosen as the scavengers for  $\cdot\text{OH}$ ,  $\cdot\text{O}_2^-$ , and  ${}^1\text{O}_2$ , respectively.<sup>15</sup> And MeOH was used to simultaneously quench  $\cdot\text{OH}$  and  $\text{SO}_4^{\cdot-}$ .<sup>17</sup> Apparently, both TBA and MeOH could strongly inhibit OTC degradation in the HEF/UV system, with MeOH-induced inhibition slightly higher than TBA. This indicated that both  $\cdot\text{OH}$  and  $\text{SO}_4^{\cdot-}$  were involved in the degradation process of OTC. Whereas the contribution of  $\text{SO}_4^{\cdot-}$  may be negligible, as evidenced by the fact that increasing the  $\text{Na}_2\text{SO}_4$  concentrations did not significantly improve the process efficiency. When the  $\text{Na}_2\text{SO}_4$  concentration was even higher than 100 mM, the degradation rate was almost unchanged (Fig. S13†). Consistent with the absence of  $\text{DMPO}\cdot\text{O}_2^-$  signal in the EPR results, the addition of BQ hardly affected the degradation of OTC, revealing that  $\cdot\text{O}_2^-$  was not involved in the oxidation process. Despite the obvious  $\text{TEMP}\cdot{}^1\text{O}_2$  signal in the EPR spectrum, the degradation kinetics of OTC decreased only slightly from  $0.24409\text{ min}^{-1}$  to  $0.22795\text{ min}^{-1}$  in the presence of TEMP, which may be due to the rapid deterioration of the  ${}^1\text{O}_2$  production rate with the reaction time (Fig. S12†). Moreover, similar results to the above can still be observed in Fig. S14† when changing the doses of different quenchers. Note that the contribution of potential chlorine radicals ( $\cdot\text{Cl}$ ) and high-valent iron species ( $\text{Fe(IV)}$ ,  $\text{Fe(V)}$ , and  $\text{Fe(VI)}$ ) can also be excluded, since no corresponding signals ( $\text{DMPO}\cdot\text{Cl}$ ) were detected in all EPR spectra (Fig. 4) and addition of dimethyl sulfoxide (DMSO) (a quencher for high-valent iron species) did not significantly affect the degradation kinetics of OTC (Fig. S15†). Overall, these facts reflect the contribution of  $\cdot\text{OH}$ ,  $\text{SO}_4^{\cdot-}$ , and  ${}^1\text{O}_2$  to the degradation of OTC, with  $\cdot\text{OH}$  playing a dominant role. This is also supported by the fact that the mineralization rates of OTC in different systems (Fig. 4e) almost coincide with the order of intensity of  $\text{DMPO}\cdot\text{OH}$ . The contradiction between the mineralization rate (Fig. 4e) and the  $\text{DMPO}\cdot\text{OH}$  signal intensity (Fig. 4a) of the UV/ $\text{H}_2\text{O}_2$  system and HEF system may be related to the difference in the evolution of  $\cdot\text{OH}$  production with reaction time. As depicted in Fig. 4f, the UV/ $\text{H}_2\text{O}_2$  system contributed to a gradually enhanced  $\cdot\text{OH}$  concentration with the reaction time, while the HEF system showed an opposite trend. This is precisely the result of the scavenging of  $\cdot\text{OH}$  by  $\text{H}_2\text{O}_2$  in the later stage of the dual-cathode HEF reaction discussed in section 3.2.

### 3.4. Assessment of practical application potential

The practical application potential of the constructed HEF/UV tandem system was evaluated from multiple perspectives.

Fig. 5a shows that refractory organic compounds with different chemical structures (tetracycline (TC), ranitidine (RNTD), and sulfamethoxazole (SMX)) can all be effectively degraded in this HEF/UV process, demonstrating its versatility and universality. In addition, the effect of real water matrices (tap water, river water, and lake water) was also evaluated. The OTC degradation rate decreased to varying degrees in this tandem system compared to the deionized water background, as shown in Fig. 5b. This phenomenon occurred because of the presence of complex inorganic anions (especially  $\text{Cl}^-$ ) and dissolved organic matter in natural waters (see Table S2† for water quality parameters of different real water matrices), which were well established as  $\cdot\text{OH}$  scavengers and will strongly affect the degradation efficiency of organic molecules.<sup>35</sup> Despite the reduced performance, it is still acceptable because the complete degradation of OTC within 60 min was achieved in different natural waters.

Service life is critical to the large-scale application of water treatment technologies, for which successive cycles of OTC degradation experiments in the HEF/UV system were performed (Fig. 5c and d). Both the degradation kinetics and mineralization rate of OTC showed a slight decrease after 10 runs. Considering the robust durability of the ADC electrode and UV lamp, the fading of the oxidation capacity of this tandem system was identified to originate from the gradual leaching of Fe ions from the surface of the FeOCl/GF catalytic cathode (Fig. S16,†  $\sim 1.2\text{ mg}$  in each run). Therefore, the development of innovative and practical fabrication strategies to enhance the stability of catalytic cathodes under realistic harsh electrolysis conditions is suggested to be a priority for future research. Fig. 5d also shows the residual  $\text{H}_2\text{O}_2$  concentration corresponding to each cycle, and only about  $40\text{ mg L}^{-1}$  of unactivated  $\text{H}_2\text{O}_2$  was detected in the HEF/UV effluent. Meanwhile, although nearly half of the degradation intermediates were predicted to be more toxic than OTC in the early stages of remediation, this HEF/UV tandem system still enabled a detoxification process for OTC as the oxidative conversion of these intermediates proceeded (Fig. S17, S18 and Tables S3, S4†). These abovementioned characteristics allowed to greatly reduce the environmental risk of OTC-containing sewage to aquatic ecosystems. Nonetheless, follow-up studies are recommended to examine the intermittent power supply mode (*i.e.*, interruption of electric current when OTC is almost completely degraded at 20 min) to further eliminate the  $\text{H}_2\text{O}_2$  residue and minimize energy consumption.

To further illustrate the superiority of the HEF/UV tandem system, a comparison of the  $k$  values for OTC degradation with other advanced oxidation-based technologies was carried out. As shown in Fig. 5e, HEF/UV probably represents the state-of-the-art catalytic performance with corresponding  $k$  values 2.7 to 48.4-fold higher than other systems,<sup>6,15,36–45</sup> suggesting the significant synergy between electro- and photo-catalysis. In view of the excellent performance of the HEF/UV tandem system, its feasibility for real industrial antibiotic wastewater treatment was evaluated. Wastewater samples were obtained from an antibiotic pharmaceutical factory (CP group,

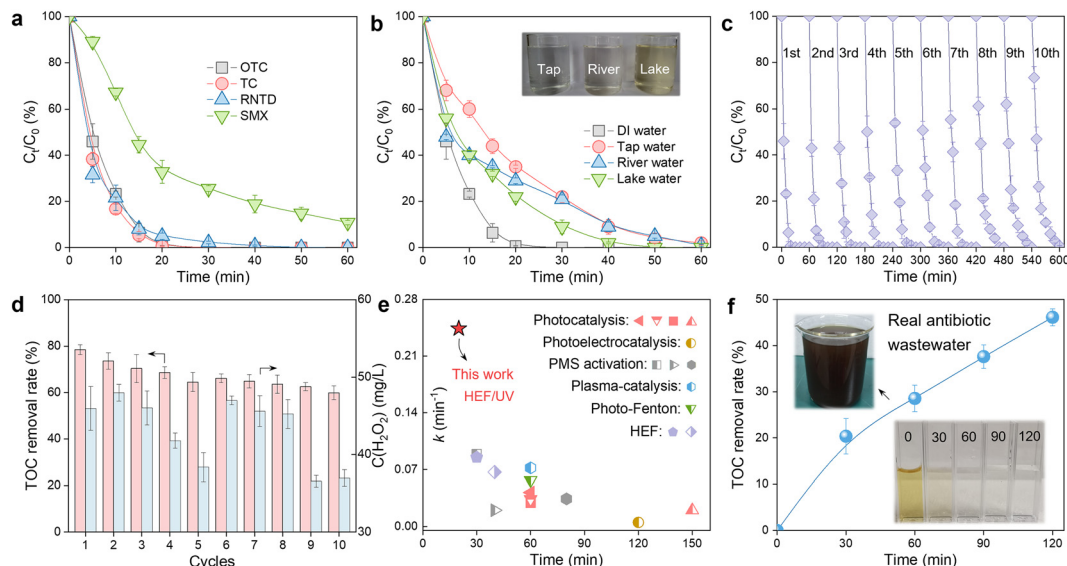


**Fig. 5** Practicability of the dual-cathode HEF and UV radiation tandem system. Evaluation of the universality of the HEF/UV tandem system in terms of (a) contaminant species and (b) natural water matrix background; durability of the HEF/UV tandem system over 10 consecutive runs: (c) OTC degradation and (d) TOC removal rate and H<sub>2</sub>O<sub>2</sub> residue (conditions: [OTC] = 20 mg L<sup>-1</sup>, pH = 4,  $I_{\text{ADC}} = 100 \text{ mA cm}^{-2}$ ,  $I_{\text{FeOCl/GF}} = 5 \text{ mA cm}^{-2}$ , and UV = 6 W); (e) comparison of OTC degradation performance between different AOP technologies reported in the literature and the HEF/UV tandem system in this study; and (f) treatment of real antibiotic wastewater using the HEF/UV tandem system (conditions:  $I_{\text{ADC}} = 100 \text{ mA cm}^{-2}$ ,  $I_{\text{FeOCl/GF}} = 5 \text{ mA cm}^{-2}$ , and UV = 6 W).

Zhengzhou, China), and the main water quality parameters are shown in Table S5.† Note that this real antibiotic wastewater is characterized by high salinity (conductivity up to 5030  $\mu\text{S cm}^{-1}$ ), for which the treatment process was performed without any supporting electrolyte addition. After 120 min, the treated wastewater became clear and transparent with a TOC removal rate of nearly 50%, even without pre-adjustment of the solution pH (Fig. 5f). Endowed with the aforementioned merits, the proposed HEF/UV tandem system may be regarded as a powerful solution for distributed water pollution remediation, due to its reagent- (*i.e.*, catalyst dosing and oxygen aeration) and oxidant-free philosophy of green chemistry.

## 4. Conclusions

In summary, a coupled system of a dual-cathode HEF process in series with UV radiation was developed for efficient distributed water pollution control. In the dual-cathode electrolysis unit, H<sub>2</sub>O<sub>2</sub> was first efficiently produced *in situ* at the ADC without aeration and then rapidly converted into active free radicals at the highly loaded FeOCl/GF catalytic cathode. The optimal operating current densities of the two cathodes were experimentally verified to be different (100 mA cm<sup>-2</sup> at ADC and 5 mA cm<sup>-2</sup> at FeOCl/GF), thus enabling simultaneous efficient 2e<sup>-</sup> ORR, H<sub>2</sub>O<sub>2</sub> activation and Fe(III) electroreduction. Importantly, the underutilized H<sub>2</sub>O<sub>2</sub> remaining in the HEF effluent will continue to be activated in the UV irradiation module, resulting in the elimination of the risk of oxidant residues and helping in further improving the degradation

efficiency. The current density applied to the ADC has a significant impact on the synergy between the electro- and photo-catalysis subprocesses in the HEF/UV tandem system. For  $I_{\text{ADC}} < 100 \text{ mA cm}^{-2}$ , the deployment of the UV module cannot eliminate the wasting reaction of  $\cdot\text{OH}$  heterogeneously produced at the FeOCl/GF cathode with H<sub>2</sub>O<sub>2</sub> produced at the ADC, while for  $I_{\text{ADC}} \geq 100 \text{ mA cm}^{-2}$ , UV photolysis of relatively high concentrations of H<sub>2</sub>O<sub>2</sub> in the HEF effluent will generate considerably homogeneous  $\cdot\text{OH}$ , which can outcompete the above wasting reactions by dimerization with heterogeneous  $\cdot\text{OH}$  at the FeOCl/GF cathode. The HEF/UV tandem strategy proposed in the present work offers an efficient, green and residual oxidant-free wastewater treatment solution, which is promising especially for distributed wastewater treatment.

## Conflicts of interest

There are no conflicts to declare.

## Acknowledgements

Financial support from the National Natural Science Foundation of China (52170041), the Tsinghua SIGS Start-up Funding (QD2020002N), the Cross-disciplinary Research and Innovation Fund (JC2022006), the Key Research and Development Program of Zhejiang Province (2023C03148) and the Committee of Science and Technology Innovation of Shenzhen (JCYJ20190813163401660) is gratefully acknowledged.

## References

- 1 B. C. Hodges, E. L. Cates and J. H. Kim, *Nat. Nanotechnol.*, 2018, **13**, 642–650.
- 2 J. M. Barazesh, T. Hennebel, J. T. Jasper and D. L. Sedlak, *Environ. Sci. Technol.*, 2015, **49**, 7391–7399.
- 3 I. Sirés and E. Brillas, *Curr. Opin. Electrochem.*, 2021, **27**, 100686.
- 4 S. O. Ganiyu, M. Zhou and C. A. Martínez-Huitle, *Appl. Catal., B*, 2018, **235**, 103–129.
- 5 C. Trelu, M. Rivallin, S. Cerneaux, C. Coetsier, C. Causserand, M. A. Oturan and M. Cretin, *Chem. Eng. J.*, 2020, **400**, 125936.
- 6 L. Cui, X. Zhao, H. Xie and Z. Zhang, *ACS Catal.*, 2022, **12**, 13334–13348.
- 7 E. Brillas, I. Sirés and M. A. Oturan, *Chem. Rev.*, 2009, **109**, 6570–6631.
- 8 S. Cheng, C. Shen, H. Zheng, F. Liu and A. Li, *Appl. Catal., B*, 2020, **269**, 118785.
- 9 L. Cui, Z. Li, Q. Li, M. Chen, W. Jing and X. Gu, *Chem. Eng. J.*, 2021, **420**, 127666.
- 10 F. Xiao, Z. Wang, J. Fan, T. Majima, H. Zhao and G. Zhao, *Angew. Chem., Int. Ed.*, 2021, **60**, 10375–10383.
- 11 P. Cao, X. Quan, K. Zhao, S. Chen, H. Yu and Y. Su, *Environ. Sci. Technol.*, 2020, **54**, 12662–12672.
- 12 Q. Zhang, M. Zhou, X. Du, P. Su, W. Fu and G. Song, *Chem. Eng. J.*, 2022, **429**, 132436.
- 13 S. Cheng, H. Zheng, C. Shen, B. Jiang, F. Liu and A. Li, *Adv. Funct. Mater.*, 2021, **31**, 2106311.
- 14 P. Su, M. Zhou, G. Ren, X. Lu, X. Du and G. Song, *J. Mater. Chem. A*, 2019, **7**, 24408–24419.
- 15 L. Cui, M. Sun and Z. Zhang, *Chem. Eng. J.*, 2022, **450**, 138263.
- 16 F. Deng, S. Li, Y. Cao, M. A. Fang, J. Qu, Z. Chen and S. Qiu, *J. Power Sources*, 2020, **466**, 228342.
- 17 Q. Zhang, H. Yin, P. Su, W. Fu, G. Song and M. Zhou, *Chem. Eng. J.*, 2022, **444**, 136590.
- 18 D. Wang, J. Hu, B. Liu, H. Hou, J. Yang, Y. Li, Y. Zhu, S. Liang and K. Xiao, *J. Hazard. Mater.*, 2021, **412**, 125269.
- 19 I. Sánchez-Montes, G. O. S. Santos, T. O. Silva, R. Colombo and M. R. V. Lanza, *J. Cleaner Prod.*, 2023, **392**, 136242.
- 20 D. Sánchez-Quiles and A. Tovar-Sánchez, *Environ. Sci. Technol.*, 2014, **48**, 9037–9042.
- 21 J. Xu, X. Zheng, Z. Feng, Z. Lu, Z. Zhang, W. Huang, Y. Li, D. Vuckovic, Y. Li, S. Dai, G. Chen, K. Wang, H. Wang, J. K. Chen, W. Mitch and Y. Cui, *Nat. Sustain.*, 2021, **4**, 233–241.
- 22 Q. Zhang, M. Zhou, G. Ren, Y. Li, Y. Li and X. Du, *Nat. Commun.*, 2020, **11**, 1731.
- 23 M. Sun, C. Chu, F. Geng, X. Lu, J. Qu, J. Crittenden, M. Elimelech and J.-H. Kim, *Environ. Sci. Technol. Lett.*, 2018, **5**, 186–191.
- 24 S. O. Ganiyu, T. X. Huong Le, M. Bechelany, G. Esposito, E. D. van Hullebusch, M. A. Oturan and M. Cretin, *J. Mater. Chem. A*, 2017, **5**, 3655–3666.
- 25 C. H. Han, H. D. Park, S. B. Kim, V. Yargeau, J. W. Choi, S. H. Lee and J. A. Park, *Water Res.*, 2020, **172**, 115514.
- 26 H. Dong, B. Dong, L. Sun, Z. Chi, M. Wang and H. Yu, *Chem. Eng. J.*, 2020, **390**, 124650.
- 27 D. Guo, Y. Liu, H. Ji, C. C. Wang, B. Chen, C. Shen, F. Li, Y. Wang, P. Lu and W. Liu, *Environ. Sci. Technol.*, 2021, **55**, 4045–4053.
- 28 X. Du, P. Su, W. Fu, Q. Zhang and M. Zhou, *Electrochim. Acta*, 2022, **412**, 140122.
- 29 P. Su, W. Fu, Z. Hu, J. Jing and M. Zhou, *Appl. Catal., B*, 2022, **313**, 121457.
- 30 S. Pan, X. Guo, R. Li, H. Hu, J. Yuan, B. Liu, S. Hei and Y. Zhang, *Sep. Purif. Technol.*, 2022, **300**, 121909.
- 31 Q. V. Ly, L. Cui, M. B. Asif, W. Khan, L. D. Nghiem, Y. Hwang and Z. Zhang, *Water Res.*, 2023, **230**, 119577.
- 32 Z. Liu, W. Hao, C. Yuan, W. Ruan, W. Jiang and F. Teng, *J. Water Process Eng.*, 2022, **48**, 102912.
- 33 Y. Zhao, M. Sun, X. Wang, C. Wang, D. Lu, W. Ma, S. A. Kube, J. Ma and M. Elimelech, *Nat. Commun.*, 2020, **11**, 6228.
- 34 Y. Jin, Y. Shi, Z. Chen, R. Chen, X. Chen, X. Zheng, Y. Liu and R. Ding, *Appl. Catal., B*, 2020, **267**, 118730.
- 35 Y. Q. Gao, J. Zhang, C. Li, F. X. Tian and N. Y. Gao, *Chemosphere*, 2020, **243**, 125325.
- 36 M. Li, J.-F. Yan, Z.-X. Zhang, W. Han, S.-Q. Zhou, K. L. Yeung and C.-H. Mo, *Environ. Sci.: Nano*, 2022, **9**, 4214–4232.
- 37 Y. Chen, R. Yin, L. Zeng, W. Guo and M. Zhu, *J. Hazard. Mater.*, 2021, **412**, 125256.
- 38 Y. Yang, G. Zeng, D. Huang, C. Zhang, D. He, C. Zhou, W. Wang, W. Xiong, X. Li, B. Li, W. Dong and Y. Zhou, *Appl. Catal., B*, 2020, **272**, 118970.
- 39 Y. Liu, X. Wang, Q. Sun, M. Yuan, Z. Sun, S. Xia and J. Zhao, *J. Hazard. Mater.*, 2022, **424**, 127387.
- 40 D. Liu, M. Li, X. Li, F. Ren, P. Sun and L. Zhou, *Chem. Eng. J.*, 2020, **387**, 124008.
- 41 H. Guo, Y. Wang, X. Yao, Y. Zhang, Z. Li, S. Pan, J. Han, L. Xu, W. Qiao, J. Li and H. Wang, *Chem. Eng. J.*, 2021, **425**, 130614.
- 42 J. Qin, S. Ye, K. Yan and J. Zhang, *J. Colloid Interface Sci.*, 2022, **607**, 1936–1943.
- 43 J. Ni, D. Liu, W. Wang, A. Wang, J. Jia, J. Tian and Z. Xing, *Chem. Eng. J.*, 2021, **419**, 129969.
- 44 W. Zhao, Q. Dong, C. Sun, D. Xia, H. Huang, G. Yang, G. Wang and D. Y. C. Leung, *Chem. Eng. J.*, 2021, **409**, 128185.
- 45 H. Y. Liu, C. G. Niu, H. Guo, C. Liang, D. W. Huang, L. Zhang, Y. Y. Yang and L. Li, *J. Colloid Interface Sci.*, 2020, **576**, 264–279.